Solid-State CMAS Corrosion of an EB-PVD YSZ Coated Turbine Blade: Zr^{4+} Partitioning and Phase Evolution

P. Mechnich & W. Braue

This is the authors version of the article published in the

Journal of the American Ceramic Society Vol. 98 (2015) pages 296–302

DOI: 10.1111/jace.13241

Solid-state CMAS corrosion of an EB-PVD YSZ coated turbine blade: Zr^{4+} partitioning and phase evolution

Peter Mechnich* and Wolfgang Braue

German Aerospace Center (DLR)

Institute of Materials Research

51147 Cologne, Germany

***corresponding author, peter.mechnich@dlr.de**

Abstract

The corrosion of an ex-service 7-YSZ coated high-pressure turbine blade by Si-undersaturated, Fe-,Ti-rich CMAS (FT-CMAS) was investigated. The constituents of the FT-CMAS deposit and its synthetic laboratory counterpart are identified by means of analytical SEM and XRD. FT-CMAS mainly consists of rhönite-, melilite-, and clinopyroxene-type solid solutions. FT-CMAS reacts with the 7-YSZ thermal barrier coating (TBC) to a continuous layer of a Ca,Zr-rich garnet phase also known as kimzeyite. The microstructural analysis indicates that kimzeyite has formed via solid-state reaction. The formation of kimzeyite was studied in laboratory using YSZ/ FT-CMAS diffusion couples and powder compacts. Experiments provide strong evidence that kimzeyite is forming predominantly from YSZ and melilite whereas clinopyroxene and especially rhönite appear relative stable versus YSZ. The preferred kimzeyite formation from melilite and YSZ is explained by the availability of 6-fold coordinated lattice sites for Zr^{4+} upon melilite decomposition and subsequent garnet crystallization.

Introduction

The ingestion of airborne mineral dust defines a serious threat to aero-engine performance and service life. The thermal barrier coatings (TBC) suffer from hot-corrosion associated with the accumulation and infiltration of molten or partially molten mineral particles. The melt infiltration of TBCs promotes a reduction in compliance and eventually spallation of the TBC from turbine blades, hence marks a limitation to the service life of turbine engines. Over the years there has been considerable effort to assess thermochemical and thermomechanical aspects of TBC degradation by ingested mineral particles, which is commonly referred to as “CMAS”-corrosion. A recent comprehensive review of CMAS-related phenomena is given by Levi et al.[1]

The blades and vanes of the 1st stage of the high-pressure turbine (HPT) are ideally suited for similar case studies as their surfaces are directly exposed to the corrosive combustion gases and impingement of airborne particles. To date only a few field studies on CMAS-corroded HPT blades with state-of-the-art TBC (Y_2O_3 stabilized ZrO_2, YSZ) are available in open literature. Such TBC are typically manufactured by electron-beam vapor deposition (EB-PVD). Vidal-Sétif et al. investigated an ex-service HPT-blade from a military engine and described the thermochemical decomposition of the EB-PVD YSZ TBC in a Fe-rich CMAS environment.[2] Mercer et al. used an ex-service blade to study the delamination of CMAS-infiltrated EB-PVD YSZ TBC. They focused their work on fracture mechanics and derived a “cold shock” damage mechanism.[3]

In a previous work we have analysed an ex-service 1st stage HPT airfoil of a Pratt & Whitney PW 4000 aeroengine with a EB-PVD YSZ TBC fully infiltrated by $CaSO_4$

(anhydrite).[4] A CMAS deposits with a high CaO-to-SiO_2 ratio and significant Fe and Ti concentrations, was found to trigger the formation of a double corrosion layer consisting of $CaZrO_3$ and a kimzeyite-type garnet phase (Ca, $Mg)_3(Zr,Ti,Fe)_2(Al,Fe,Si)_3O_{12}$. Thus an expanded "FT-CMAS" system was introduced. In the present work we have investigated an ex-service EB-PVD YSZ coated 1st stage HPT blade from a Pratt & Whitney PW 2000 aeroengine with a similar "FT-CMAS" deposit. In contrast to our previous study, the present PW 2000 blade happened to experience limited $CaSO_4$ infiltration only, thus offering the opportunity to study CMAS corrosion of YSZ without contribution of $CaSO_4$. Our research is focusing on phase formation on the pressure surface of the CMAS-corroded HPT blade. Observations are corroborated by laboratory experiments using EB-PVD 7-YSZ coatings with artificial CMAS powder deposits.

Experimental Procedure

The ex-service high-pressure turbine blade (HPT) was kindly provided by MTU Aeroengines Maintenance (Hannover, Germany). Similar aeroengines are employed for example in Boeing 757 or Boeing C17 type aircrafts. Information on operation conditions are not available, however a service life of ten thousand hours and beyond is likely.

The CMAS corrosion scenario was accessed through a combination of scanning electron microscopy (SEM), energy dispersive spectroscopy (EDS) and X-ray diffraction (XRD) (see schematic in figure 1). On the basis of the blade's bulk CMAS composition a laboratory CMAS powder was synthesized (1250 °C/10 h) from Al-, Ca-, Mg-, and Fe-nitrates and nanosized SiO_2 and TiO_2 powders (Merck, Darmstadt,

Germany). Individual phases were analysed by EDS spot measurements, re-synthesized as single phases, and confirmed by means of XRD.

CMAS/7-YSZ diffusion couples were prepared by depositing about 20 mg/cm^2 of laboratory CMAS on top of approximately 250 μm thick EB-PVD coatings (electron-beam physical vapor deposition, von Ardenne Anlagentechnik, Dresden, Germany). 7 mol-% (4 wt-%) Y_2O_3-stabilized ZrO_2 (TZ-4Y, Tosoh Chemicals, Tokyo, Japan) was used as reference powder. All heat treatments were performed in a chamber furnace in air (HTC 03/15, Nabertherm, Bremen, Germany).

SEM analyses were performed in a DSM Ultra 55 scanning electron microscope (Carl Zeiss NTS, Wetzlar, Germany) equipped with INCA energy-dispersive spectroscopy (Oxford Instruments, Abingdon, UK). XRD analyses were performed in a D8 Advance diffractometer with CuKα radiation and Lynxeye™ detector (Bruker AXS, Karlsruhe, Germany). Powders were measured in conventional Bragg-Brentano geometry while the PW 2000 blade was analyzed in parallel beam geometry using a Göbel mirror.

Results & Discussion

Corrosion scenario of the PW 2000 HPT blade

The TBC surfaces of the ex-service PW 2000 HPT blade exhibit significant tarnishing caused by deposited “CMAS” mineral particles. The major part of dark-brown CMAS is accumulated on the central pressure surface region (fig 2). The significantly lighter contrasting downstream of the cooling boreholes is probably due to combined effects of less CMAS deposition and lower surface temperatures. Significant TBC erosion is mainly observed at the blade tip, where an area of approximately 1 cm^2 has spalled

off. While the TBC is virtually undamaged at the trailing edge, a small part of the leading edge has spalled off. A cross-section was performed at the center of the pressure surface close to the spalled area. The SEM image (Fig.3) shows the typical columnar microstructure of EB-PVD YSZ. The approximately 50 μm thick CMAS deposit exhibits a multiphase, fully crystalline microstructure. The chemical composition of the multiphase overlay was derived via EDS area analysis. The deposit is mainly composed of classical CMAS-constituents CaO (29.8 mol%), MgO (11.3 mol%), Al_2O_3 (11.1 mol%), SiO_2 (23.9 mol%). Additionally substantial amounts of FeO (19.1 mol%), TiO_2 (2.1 mol%), and ZrO_2 (2.5 mol%) are detected. Note that the Fe analysis given as FeO is simply for technical reasons and does not imply the presence of Fe^{2+}. ZrO_2 is likely due to dissolution of the YSZ TBC and therefore not considered as real CMAS-constituent. The same would apply for Y_2O_3; however the Y content was generally below the EDS detection limit. The small concentration of Ni (0.3 mol%) is best attributed to wear of Ni-based alloy of the compressor**.** In order to recognize the significant amounts of Fe and Ti, the deposit composition is referred to as “FT-CMAS”.

The FT-CMAS/YSZ interface is characterized by a few μm thick continuous overlay and a similar contrasted, approximately 40 μm deep infiltration of the intercolumnar porosity. Towards the bondcoat an approximately 30 μm thick area with pronounced open porosity is obvious. In the TBC root zone porosity appears to be filled again. The infiltration sequence is rationalized by Ca-Kα_1, Si-Kα_1 and S-Kα_1 EDS maps given as inset in figure 3: Only calcium and sulfur are detected in the TBC root zone, proving that the lower pore filling is consisting of pure anhydrite ($CaSO_4$). Recently we observed complete $CaSO_4$-infiltration of intercolumnar TBC porosity of a 1st stage HPT-blade which can be rationalized as gas-phase transport and subsequent

condensation in cooler TBC regions.[5] Silicon and calcium are evidently major constituents of the overlay and the upper pore filling. Due to the limited $CaSO_4$ infiltration it is anticipated that the corrosion zone at the FT-CMAS/YSZ interface has formed without direct contribution of $CaSO_4$.

Phase paragenesis of the PW 2000 corrosion zone

In analogy to our previous work[4] a laboratory FT-CMAS was synthesized at 1250°C, which is considered a plausible estimate for TBC peak surface temperatures in engine operation. The qualitative XRD phase analysis revealed that as-synthesized laboratory FT-CMAS is fully crystalline**,** consisting of rhönite (R_L), melilite (M_L), and clinopyroxene (C_L) (Fig. 4 (i); note subscript $_L$ for “laboratory”). Due to additional XRD reflections of tetragonal YSZ (tZ) the interpretation of the XRD profile collected at the blade’s pressure surface is more difficult. EB-PVD YSZ exhibits strong texture with weak (101) while (002) and (110) peaks are dominating. Nevertheless melilite (M_B) as well as rhönite (R_B) are unambiguously identified, but there is no clear evidence for clinopyroxene (Fig. 4 (ii); note subscript $_B$ for “blade”). The strong XRD peak at 25.5° 2-θ (A) can be assigned to anhydrite $CaSO_4$.

To our best knowledge this is the first report of rhönite in the context of CMAS corrosion. Rhönite is an accessory rock-forming mineral typically occurring in Fe-rich, low-silica environments such as basalts.[6] Among the most prominent natural occurrences of rhönite are Ca-,Al-rich inclusions found in the Allende meteorite and inclusions of augite grains of lunar regolith.[7,8] Rhönite has formerly been categorized as a member of the aenigmatite (aenigmatite: $Na_2TiFe^{2+}_5Si_6O_{20}$) or the aenigmatite-rhönite mineral group, but more recently is considered as an equal member of the highly complex and variable sapphirine group of chain silicates.[9-11] The crystal

structure analysis of a natural rhönite revealed its triclinic symmetry with an idealized formula $Ca_4[(Mg,Fe^{2+})_8Fe^{3+}{}_2Ti_2]Al_6Si_6O_{40}$.[12] The rhönite structure easily accommodates various cation species.[13] On the other hand, there even exist Fe-free or Ti-free rhönites, respectively.[14,15]

Similar synthetic, rhönite-type phases are also technologically relevant: sinter-ores employed in blast-furnace iron-making are including so-called “silico-ferrite” phases such as “SFCA” (Si, Fe, Ca, Al) and “SFCAM” (Si, Fe, Ca, Al, Mg) both being structurally closely related to rhönite.[16,17]

Melilite ($Ca_2(Mg_xAl_{1-x})(Si_{1+x}Al_{1-x})O_7$) refers to tetragonal solid solutions of the end members akermanite ($Ca_2MgSi_2O_7$) and gehlenite ($Ca_3Al_2SiO_7$).[18] In Fe-rich environments, melilite solid solutions can also include the Fe-analogues ferrigehlenite ($Ca_3Fe_2SiO_7$) or ferroakermanite ($Ca_2MgFe_2O_7$).[19,20] Previously we have found Fe-holding melilite as a major constituent of a FT-CMAS deposit of a HPT blade.[4]

Clinopyroxenes are abundant rock-forming minerals which typically include solid solutions of end-members such as diopside ($CaMgSi_2O_6$) or hedenbergite ($CaFeSi_2O_6$). Al-rich esseneite ($CaFe^{3+}AlSiO_6$) has been described as constituent of high-temperature metamorphic rocks.[21]

The morphology of co-existing phases in laboratory FT-CMAS and the corresponding phases in the corrosion zone of the HPT-blade was studied by SEM and EDS.

Figure 5 shows a polished cross section of laboratory FT-CMAS, while figure 6 shows a close-up of the PW 2000 corrosion zone. Note that both FT-CMAS microstructures are devoid of glassy phases at triple grain junctions.

The corresponding EDS spot analyses and of solid solution calculations are compiled in table 1. Note that laboratory phases and blade phases are again marked by “$_L$” and “$_B$” subscripts, respectively.

Large isometric crystals of typically 10 μm and beyond with high relief are identified as rhönite (R_L, R_B). From the quantitative EDS analysis (table 1) the chemical composition of R_B is close to that of synthetic R_L: while contents of Mg, Al, Si and Ti are similar the Ca content is higher and the Fe content is lower, respectively. Zr is generally below detection limit. On the basis of a generalized rhönite structure (table1) and an allocation of the cations on plausible lattice sites, it is possible to calculate approximated rhönite-type solid solutions. Note that the assumed substitutions $Ti^{4+} \rightarrow Fe^{3+}$ and $Si^{4+} \rightarrow Al^{3+}$ require a slight oxygen deficiency (1.5 oxygen per unit cell) for achieving charge balance.

Unlike rhönite, both melilites (M_L, M_B) appear as featureless matrix phase (Figs. 5, 6). Although the EDS analysis of melilite M_B revealed a differing content of Al and Ca, respectively, all other cation concentrations remain quasi identical (table 1). EDX quantification and cation allocation allows for approximating both M_L and M_B as a solid solution of approximately 50% gehlenite, 10% ferrigehlenite and 40 % akermanite, respectively. Similar melilites were found upon firing of industrial, Ca-rich silicate ceramics such as clay bricks.[22] Note that both M_L and M_B are virtually free of Ti and Zr.

In laboratory FT-CMAS, clinopyroxene C_L is forming small, slightly darker contrasted crystals frequently growing adjacent to rhönite R_L (Fig. 5). Again the EDX quantification and cation allocation in a generalized structure were employed for an approximation of a charge-balanced clinopyroxene stoichiometry. Note that the clinopyroxene EDS analyses in table 1 requires cation position $T^{[4]}$ being fully occupied by Si and Al and position $A^{[8]}$ fully occupied by Ca, respectively. Therefore Mg, Fe, and minor Ti, Zr were allocated to position $B^{[6]}$ only. A simplified model solid solution for C_L would consist of 60% esseneite, 30% diopside and 10 % hedenbergite (table 1). A rather similar clinopyroxene having a composition of

$Ca_{0.96}(Al_{0.20}Fe_{0.35}Mg_{0.44})(Al_{0.20}Fe_{0.08}Si_{0.70})_2O_{6.12}$ has been described in literature.[23] The PW 2000 blade exhibits a different scenario: interestingly C_B seems to be is accumulated in a layer close to the TBC interface (fig 5). Compared to C_L C_B holds approximately 50% less Fe and 25 % more Al and Mg, respectively (table 1).

In contrast to XRD analysis (Fig. 4) SEM of the laboratory FT-CMAS analysis reveals an additional crystalline phase "T_L" appearing as light-gray contrasted grains with sizes typically below 5 μm (Fig. 5). On the basis of EDS spot analysis and subsequent single synthesis phase "T_L" could be identified as a Ti-rich, garnet-type solid solution (table 1). Ti-rich garnets, such as melanites and schorlomites, are also referred to as Ti-andradites with the empirical formula $Ca_3Fe_2(Si_{0.5}Ti_{0.5})_3O_{12}$.[24] T_L is easily approximated by a 50:50 mol% solid solution of Ti-andradite and grossular ($Ca_3Al_2Si_3O_{12}$). Remarkably similar garnets have been reported elsewhere.[25] The absence of garnet reflections in the XRD profile (Fig. 4) is apparently due to peak overlap: for example, the characteristic XRD reflections of Ti-andradite (ICDD PDF-2; #78-0319)[26] 220 (d=0.423 nm), 400 (d=0.306 nm) and 422 (d=0.273 nm) coincide with strong melilite XRD-reflections 101 (d=0.422 nm), 201 (d=0.307 nm) and 211 (d=0.285 nm), respectively.

The PW 2000 blade exhibits a reaction layer between the EB-PVD YSZ coating and the crystalline FT-CMAS overlay (Fig. 6). EDS analysis as well as single-phase synthesis unambiguously prove that newly formed K_{B1} is a Zr-rich garnet-type solid solution. Such garnets are commonly referred to as kimzeyite with an empirical formula $Ca_3(Zr,Ti,Fe,)_2(Al,Fe,Si)_3O_{12}$.[27,28] The approximation of the K_{B1} solid solution (table 1) required an allocation of Fe^{3+} to tetrahedral T sites, resulting in an almost equivalent distribution of Fe^{3+} on octahedral B and tetrahedral T, respectively.

An additional phase is appearing as light-gray contrasted grains having a size 0.5-1 μm and is typically growing adjacent to the clinopyroxene (C_B) layer or rhönite (R_B)

(white arrows in Fig. 6). The label K_{B2} is pointing out that this phase could be identified as a second kind of kimzeyite: K_{B2} is holding all available cations and the approximation of a charge balanced garnet stoichiometry is viable. A significant feature of K_{B2}, however, is a much lower Zr content (5.6%) compared to K_{B1} (14%). Moreover, K_{B2} exhibits s significant higher content of Al, therefore no Fe^{3+} had to be allocated to the T site (table 1). Figure 6 displays some monoclinic ZrO_2 (mZ) located at TBC column tips. Note that surrounding TBC pores are partially unfilled and mZ grains are in contact with kimzeyite K_{B1}. The formation of mZ may be triggered by a thin, glassy grain boundary film. However, spherulitic, (Ca-bearing) ZrO_2 grains being characteristic for YSZ dissolution and subsequent re-precipitation in excess siliceous liquid phase are not a characteristic microstructural feature.

Laboratory duplication of the PW 2000 CMAS corrosion scenario

The phase formation and microstructural evolution of the PW 2000 blade were duplicated by depositing laboratory FT-CMAS powder on an EB-PVD 7-YSZ coated alumina coupon and subsequent annealing at 1250 °C for 10 hrs. Again, the temperature of 1250°C was selected in analogy to our previous work.[4] The SEM cross section at the interface (fig. 7) reveals the formation of a pronounced reaction zone fully enveloping YSZ column tips as well infiltration of intercolumnar TBC porosity, both having a striking similarity with the PW 2000 scenario. The overlay and the pore fillings unequivocally consist of kimzeyite, referred as to K_L in the following. The average EDS analysis of K_L reveals a good agreement with K_{B1} of the PW 2000 blade (table 1). On the other hand, there is only partial “wetting” of the TBC surface by FT-CMAS, at first glance conflicting to the continuous K_L overlay. Moreover, there

are almost no melilite (M) and clinopyroxene (C) grains co-existing with K_L whereas rhönite (R) grains adjacent to K_L exhibit notable large grain sizes.

The phase evolution of the laboratory diffusion couple was corroborated by supplementary annealing experiments using 80/20 wt% powder mixtures of YSZ (TZ-4Y) and synthetic R_L C_L, and M_L, respectively. The XRD profile (i) in figure 8 reveals that R_L and tetragonal ZrO_2 (tZ) still co-exist after one hour at 1250°C. No additional XRD reflections can be detected. The C_L/TZ-4Y powder mixture (Fig. 8, profile ii) shows weak, very broad XRD peaks at 29°, 32.5° and 55.5° 2-θ which may be assigned to kimzeyite (K). Note that the tZ peak doublets (112)/(200) at 50° 2-θ and (102)/(211) at 60° 2-θ indicate a significant evolution of tZ, i.e. the tetragonality of ZrO_2 as expressed by the doublets' peak distances has seemingly decreased.

The behavior of the M_L/TZ-4Y powder mixture is evident: new kimzeyite XRD reflections (K) appear (Fig.8, profile iii). In contrast to the R_L and C_L mixtures, ZrO_2 is now existing as cubic polymorph (cZ): the tZ peak doublets (112)/(200) at 50° 2-θ and (102)/(211) at 60° 2-θ have disappeared at the expense of the (220) and (311) single peaks of cubic cZ. The tetragonal-to-cubic transformation of TZ-4Y may either be explained by incorporation of additional stabilizer such as Ca^{2+} or the relative enrichment of Y^{3+} caused by Zr^{4+} depletion due to formation of kimzeyite.

At first glance there is no evidence for the relative preference for the reaction of YSZ and melilite to kimzeyite, since rhönite and clinopyroxene offer the same cations, in particular sufficient Ca^{2+}. Accessing this observation via thermodynamic analysis or simulation of the eight-component system (Ca-Mg-Al-Si-Fe-Ti-Zr-O) is considered not very promising since all relevant phases exhibit extensive solid solubility.

Alternatively, the preferred oxygen coordination of present cations and their relative concentrations can help to rationalize the specific reactivity observed. In particular

the behavior of Zr^{4+}, typically occupying the octahedrally coordinated B-site of garnet structures[27], is considered a key to the present corrosion scenario. The total number of cation sites and their respective oxygen coordination number [CN] of the relevant crystal structures are compiled in table 2. A premise for the following considerations is the stabilization of Zr^{4+} solely on octahedrally coordinated sites ("[6]-sites").

The rhönite structure comprises a total of twelve [6]-sites, in the present case occupied by Fe^{2+}, Fe^{3+}, Ti^{4+}, and Al^{3+}. Consequently, diffusion of Zr^{4+} into the rhönite structure is hindered, as supported by the low-to-zero Zr-content of R_B (table 1). A fictional kimzeyite formation via rhönite decomposition implicates that all ([7]-coordinated) Ca^{2+} of rhönite is occupying the $A^{[8]}$-sites of the newly formed garnet. "Normalizing" the numbers of the rhönite [8]-, [6]-, and [4]-sites to three garnet $A^{[8]}$-sites yields nine [6]-sites. Only two of them need to be re-assigned to garnet $B^{[6]}$-sites, i.e. seven surplus [6]-sites remain. By analogy six [4]-cations of rhönite would translate to three tetrahedral $T^{[4]}$-sites with three surplus [4]-sites remaining. If additional Zr^{4+} is exclusively occupying [6]-sites, it would have to compete for garnet $B^{[6]}$-sites with an enormous excess of $Fe^{2+,3+}$,Ti^{4+}. Following this concept, the relative high concentration of [6]-cations ($Fe^{2+,3+}$, Ti^{4+}) in rhönite represents a too high barrier for the formation of a Zr-bearing garnet structure, in good agreement with the lack of kimzeyite in the R_L/TZ-4Y powder mixture.

A similar, fictional transformation of clinopyroxene to garnet would yield one extra [6]-site, and three extra [4]-sites, respectively. In this case only one extra [6]-cation would have to compete with Zr^{4+}, consequently the barrier for kimzeyite formation should be lower than for the rhönite case. Indeed, the only minor kimzeyite formation in the C_L/TZ-4Y powder mixture (Fig.8) supports this hypothesis.

A completely different situation exists in case of melilite: the structure includes two [8]-sites and two [4]-sites, but no [6]-sites. A fictional conversion of the "normalized"

melilite structure to a kimzeyite-type garnet is easily achieved by re-allocation of 1.5 cations, evidently Al^{3+},Fe^{3+} from $T^{[4]}$-sites to newly formed $B^{[6]}$-sites (table 2, i). Subsequently filling the 0.5 $B^{[6]}$ sites by Zr^{4+} (table 2,ii) results in the total reaction

$$1.5\ \text{Melilite} + 0.5\ Zr^{[6]}O_2 \rightarrow \text{Kimzeyite}$$

This concept may explain the enhanced formation of kimzeyite in the M_L/TZ-4Y powder mixture. The two model reactions based upon laboratory melilite M_L and pure ZrO_2 are supporting the plausibility of this concept (table 2). Note that the allocation of Mg^{2+} on $A^{[8]}$ gives rise to a higher Zr-concentration in the garnet, quite similar to the experimental observations.

From the supplementary annealing experiments it is concluded that the continuous kimzeyite layer enveloping the TBC column tips has formed preferentially at the expense of melilite while large rhönite grains represent residues of this reaction. In contrast to the PW 2000 blade (see Fig. 7) the laboratory diffusion couple does not exhibit the formation of a clinopyroxene layer separating kimzeyite and melilite. The stability considerations, however, do not rule out such a (Zr-saturated) clinopyroxene layer: even if residual rhönite is stable with respect to kimzeyite, it may react with excess melilite to clinopyroxene in the long term.

A further microstructural feature of the laboratory FT-CMAS/EBPVD 7YSZ diffusion couple is presented in figure 9 (close-up of the boxed region in figure 7). In addition to major melilite (M) and rhönite (R), the FT-CMAS overlay is holding a large number of newly formed small, Ti- and Zr-rich grains frequently exhibiting a core/rim element contrast. The inset represents an EDS line scan (normalized to Ti and Zr) across two adjacent grains (dashed arrow). The line scan proves that grains are exhibiting a Ti-rich core and a Zr-rich rim, respectively. Ti-rich cores may be assigned to initially present T_L or T_L-nuclei, rims have evidently formed by accumulation of Zr diffusing out of EB-PVD YSZ. Therefore these grains may be regarded as (early-stage)

analogues of small, isolated K_{B2} kimzeyites and may explain their occurrence distant from the FT-CMAS/YSZ interface of the PW 2000 blade (Fig. 6).

General aspects of the PW 2000 CMAS corrosion scenario

Unlike SiO_2-saturated CMAS-type corrosion scenarios, such as standard laboratory CMAS[29], neither the ex-service HPT blade nor the laboratory diffusion couples show evidence for TBC dissolution and re-precipitation of Y-depleted and Ca-containing (monoclinic) YSZ spherules. It is anticipated that YSZ dissolution/ re-precipitation requires a substantial amount of a siliceous liquid phase. The ex-service blade as well as laboratory experiments indicate that in SiO_2-undersaturated environments YSZ decomposition is occurring essentially via solid state reactions. The microstructural analyses prove that the reaction zone between YSZ TBC and FT-CMAS deposit is consisting of kimzeyite-type garnet K_{B1} which evidently is forming only in environments providing sufficient Ca and Fe. A noteworthy feature, however, is the approximately 40 μm deep infiltration of the intercolumnar porosity by K_{B1} since a significant temperature gradient is expected across the TBC thickness. The diffusion of species along EB-PVD YSZ columns is obviously high enough to enable long-term stabilization of kimzeyite even if temperatures remain well below the 1250°C estimate at the HPT blade pressure surface. A lower temperature limit of 1150°C seems plausible.

The present study is in good agreement with our previous work where a double layer consisting of a similar kimzeyite garnet and $CaZrO_3$ was found as CMAS corrosion scenario of an ex-service 7-YSZ coated, fully $CaSO_4$-infiltrated PW 4000-type HPT blade[3], emphasizing the general significance of Ca,Zr,Fe-garnets for the corrosion of 7-YSZ TBCs. In the present PW 2000 blade, however, we find no formation of $CaZrO_3$. This is confirming our assumption that $CaZrO_3$ is forming directly from

infiltrated $CaSO_4$ and YSZ above estimated 1100°C. In the present case the $CaSO_4$ pore-filling is limited to the TBC root zone and obviously did not reach the necessary temperature level for $CaZrO_3$ formation. The $CaSO_4$ infiltration at the root zone of the present TBC emphasizes the gas-phase condensation concept[5] since there is no plausibility that any "$CaSO_4$-liquid" would be able to migrate across the entire TBC thickness leaving behind a zone of open porosity. Instead, one would expect rapid "freezing" of such a liquid in the temperature gradient across the TBC thickness. The $CaSO_4$ infiltration of intercolumnuar TBC porosity is considered a global effect in turbine operation; however the underlying mechanism is still not worked out in detail and calls for more R&D efforts in future.

The large spalled TBC area is located at the center of the HPT blade where presumably particle accumulation as well as thermal load is maximal. At this point, however, the impact of "solid-state" CMAS-recession on TBC lifetime is difficult to estimate. Isothermal and thermal gradient cyclic testing of laboratory specimen will provide data comparable to results obtained for "classical" TBC corrosion induced by CMAS-melt infiltration. Physical data such as specific thermal expansion of relevant solid solutions (kimzeyite, rhönite, melilite) are required for the evaluation of mechanical stresses. The manufacturing of laboratory specimen, however, is considered difficult: the present study shows that simple deposition and annealing of FT-CMAS powders does not produce a conformal and dense TBC overlay even at 1250 °C. Advanced deposition methods, such as thermal spraying of FT-CMAS powders, may enable the duplication of real corrosion scenarios.

Conclusions

The corrosion of the investigated ex-service PW 2000 HPT blade is induced by a silica-undersaturated CMAS deposit including Fe and Ti as major constituents (FT-CMAS). FT-CMAS constituents are crystalline solid solutions such as rhönite, melilite, and clinopyroxene. The present corrosion scenario exhibits no evidence for FT-CMAS melting and YSZ dissolution/re-precipitation. Instead FT-CMAS deposits and YSZ TBC react to kimzeyite-type Ca,Zr,Fe-garnets in the solid state. Kimzeyite forms a continuous layer enveloping TBC column tips, however is also crystallizing in the topmost TBC pores. Kimzeyite forms most easily from melilite and YSZ, whereas present rhönite appears most stable versus YSZ. The preferred reaction of melilite is attributed to its significant lower concentration of transition-metal cations competing with Zr^{4+} for octahedrally coordinated garnet sites. The results emphasize that CMAS-corrosion of YSZ is possible even in absence of siliceous liquid phases and is considered as much relevant as SiO_2-saturated CMAS-corrosion.

Acknowledgement

The support by A. Ebach-Stahl and P. Watermeyer (DLR) for the preparation of the HPT blade is gratefully acknowledged.

References

[1] C. G. Levi , J. W. Hutchinson , M.-H. Vidal-Sétif, and C. A. Johnson, “Environmental degradation of thermal barrier coatings by molten deposits”, MRS Bull. 37, 932-941 (2012)

[2] M.-H. Vidal-Setif, N. Chellah, C. Rio, C. Sanchez, and O. Lavigne, “Calcium–magnesium–alumino-silicate (CMAS) degradation of EB-PVD thermal barrier coatings: Characterization of CMAS damage on ex-service high pressure blade TBCs”, Surf. Coat. Techn. 208, 39-45 (2012)

[3]C. Mercer, S. Faulhaber, A.G. Evans, and R. Darolia, ”A delamination mechanism for thermal barrier coatings subject to calcium–magnesium–alumino-silicate (CMAS) infiltration”, Acta Mater. 53, 1029–1039 (2005)

[4] W. Braue, and P. Mechnich, “Recession of an EB-PVD YSZ Coated Turbine Blade by $CaSO_4$ and Fe, Ti-Rich CMAS-Type Deposits”, J. Am. Ceram. Soc. 94[12] 4483-4489 (2011)

[5] W. Braue, P. Mechnich, and P. W. M. Peters, “The $CaSO_4$ phase in fully infiltrated electron-beam physical vapour deposited yttria stabilized zirconia top coats from engine hardware”, Mat. at High Temp. 28[4], 315-323 (2011)

[6] R. Grapes, and J. Keller, “Fe^{2+}-dominant rhönite in undersaturated alkaline basaltic rocks, Kaiserstuhl volcanic complex, Upper Rhine Graben, SW Germany”, Eur. J. Mineral. 22[2], 285-292 (2010)

[7] L. H. Fuchs, “The mineralogy of a rhönite-bearing calcium aluminium rich inclusion in the Allende meteorite, Meteoritics 13[1], 73-88 (1978)

[8] A. H. Treiman, “Rhönite in Luna 24 pyroxenes: First find from the Moon, and implications for volatiles in planetary magmas”, Am. Min. 93, 488–491(2008)

[9] B. B. Jensen, “Solid solution among members of the Aenigmatite group”, Min. Mag. 60 982-986 (1996)

[10] T. Kunzmann, “The aenigmatite-rhonite mineral group”, Eur. J. Min. 11 [4] 743-756 (2004)

[11] E. S. Grew, U. Halenius, M. Pasero, and J. Barbier, “Recommended nomenclature for the sapphirine and surinamite groups (sapphirine supergroup)”, Min. Mag. 72(4), 839–876 (2008)

[12] K. Walenka, “Zur Kristallographie des Rhönits”, Z. Krist 130, 214-230 (1969) (in german; abstract also in english)

[13] A. D. Johnston, and J. H. Stout, “Compositional variation in naturally occurring rhönite”, Am. Min. 70, 1211-1216 (1985)

[14] M. A. Cosca, R. R. Rouse, and E. J. Essene, “Dorrite [$Ca_2(Mg_2Fe^{3+}_4)(Al_4Si_2)O_{20}$], a new member of the aenigmatite group from a pyrometamorphic melt-rock”, Am. Min. 73, 1440-1448 (1988)

[15] E. Bonaccorsi, S. Merlino, and M. Pasero, “Rhonite: structural and microstructural features, crystal chemistry and polysomatic relationships”, Eur. J. Min. 2, 203-218 (1990)

[16] N. A. S. Webster, M. I. Pownceby, I. C. Madsen, and J. A. Kimpton, “Silico-ferrite of Calcium and Aluminum (SFCA) Iron Ore Sinter Bonding Phases: New Insights into Their Formation During Heating and Cooling”, Met. and Mat. Trans. B 43, 1344-1357 (2012)

[17] K Sugiyama, A. Monkawa, and T. Sugiyama, “Crystal structure of the SFCAM phase $Ca_2(CaFeMgAl)_6(FeAlSi)_6O_{20}$”, ISIJ International 45[4], 560-568 (2005)

[18] I. P. Swainson, M. T. Dove, W. W. Schmahl, and A. Putnis, “Neutron Diffraction Study of the Akermanite-Gehlenite Solid Solution Series”, Phys. Chem. Min. 19, 185-195 (1992)

[19] V. Zacek, R. Skala, M. Chlupacova, and Z. Dvorak, “Ca-Fe^{3+}-rich, Si-undersaturated buchite from Zelenky, North-Bohemian Brown Coal Basin, Czech Republic”, Eur. J. Mineral.17, 623-633 (2005)

[20] F. F. Foit Jr, R. L. Hooper, and P. E. Rosenberg, “An unusual pyroxene, melilite, and iron oxide mineral assemblage in a coal-fire buchite from Buffalo, Wyoming”, Am. Min. 72, 137-147 (1987)

[21] M. A. Cosca, and D. R. Peacor, “Chemistry and structure of esseneite ($CaFe^{3+}AlSiO_6$), a new pyroxene produced by pyrometamorphism” Am. Min. 72, 148-156 (1987)

[22] M. Dondi, G. Ercolani, B. Fabbri, and M. Marsigli, “Chemical Composition of Melilite Formed during the Firing of Carbonate-Rich and Iron-Containing Ceramic Bodies”, J. Am. Ceram. Soc. 82[2], 465-68 (1999)

[23] Y. K. Kabalov, O. Oeckler, E. V. Sokolova, A. B. Mironov, and B. V. Chesnokov, “Subsilicic ferrian aluminian diopside from the Chelyabinsk coal basin (Southern Urals) - an unusual clinopyroxene”, Eur. J. Min. 9, 617 -621 (1997)

[24] F. E. Huggins, D. Virgo, and H. G. Huckenholz, “Titanium-containing silicate garnets. II. The crystal chemistry of melanites and schorlomites”, Am. Min. 62, 646-665 (1977)

[25] A. Kühberger, T. Fehr, H. G. Huckenholz, and G. Amthauer, ”Crystal Chemistry of a Natural Schorlomite and Ti-Andradites Synthesized at Different Oxygen Fugacities”, Phys. Chem. Min. 16 734-40 (1989)

[26] Powder Diffraction File, International Center for Diffraction Data (ICDD), Newtown Square, PA.

[27] J. Ito and C. Frondel, “Synthetic Zirconium and Titanium Garnets”, Am. Min. 52, 773-781 (1967)

[28] R. Munno, G. Rossi, and C.Tadini, “Crystal chemistry of kimzeyite from Stromboli, Aeolian Islands, Italy”, Am. Min. 65, 188-191(1980)

[29] S. Krämer, J. Yang, C.G. Levi, and C.A.J. Johnson, “Thermochemical Interaction of Thermal Barrier Coatings with Molten CaO-MgO-Al_2O_3-SiO_2 (CMAS) Deposits”, *J. Am. Ceram. Soc.*, 89[10] 3167-75 (2006)

Figure Captions

Fig. 1 : Schematic of the experimental procedure adopted in this study

Fig. 2 :. Pressure surface of the ex-service 1st stage HPT blade of a PW 2000 aeroengine exhibiting CMAS particle contamination and partial TBC spallation

Fig. 3 : Polished cross-section of EB-PVD YSZ coating with CMAS overlay (SE image) showing a continuous reaction layer at the interface. The inserted Ca and Si EDS maps indicate infiltration of upper intercolumnar gaps by a siliceous phase whereas Ca and S EDS maps indicate $CaSO_4$-infiltration of the TBC root zone.

Fig. 4 : (i) XRD profile of laboratory FT-CMAS exibiting melilite (M_L), rhönite (R_L) and clinopyroxene (C_L) solid solutions. (ii) XRD profile collected from the corroded HPT blade. Beside textured tetragonal YSZ (tZ) from the TBC, melilite (M_B) as well as rhönite (R_B) are clearly detected. The peak (A) can be assigned to anhydrite. (Note subscripts $_L$ for laboratory and $_B$ for blade)

Fig. 5 : Polished cross-section (SE image) of laboratory FT-CMAS (1250 °C/ 10 h) exhibiting the specific morphologies of rhönite (R_L), melilite (M_L), and clinopyroxene (C_L). A light-contrasted, small-grained phase (T_L) is identified as Ti-rich garnet.

Fig. 6 : Polished cross-section of the EB-PVD coated HPT blade (SE image) exhibiting the specific morphologies of rhönite (R_B) and melilite (M_B). Clinopyroxene (C_B) is accumulated in a layer adjacent to the reaction zone consisting of kimzeyite-type garnet (K_{B1}). Small grains marked by arrows are also identified as kimzeyite (K_{B2}). Note the infiltration of intercolumnar gaps by K_{B1}. Partial YSZ destabilization to monoclinic ZrO_2 (m-Z) is observed at the blunted column tips.

Fig. 7 : Phase assemblage (SE contrast) from the EB-PVD YSZ/synthetic FT-CMAS diffusion couple experiment upon annealing at 1250 °C/10 h. Phases include melilite (M_L), rhönite (R_L) and newly formed kimzeyite (K_L). See Fig. 9 for close-up of boxed region.

Fig. 8 : XRD profiles collected from 80/20 wt-% powder mixtures annealed at 1250 °C/ 1h: (i) R_L/ TZ-Y4; (ii) C_L/ TZ-Y4 ; (iii) M_L/TZ-Y4. Note relative stability of rhönite R_L and preferred kimzeyite formation from YSZ and melilite M_L.

Fig. 9 : Boxed region from Fig. 7: Small precipitates frequently exhibit a pronounced core/rim structure. The normalized EDS line scan across two zoned microcrystals (dashed arrow) reveals Ti-rich cores and Zr-rich rims, respectively.

Fig.1

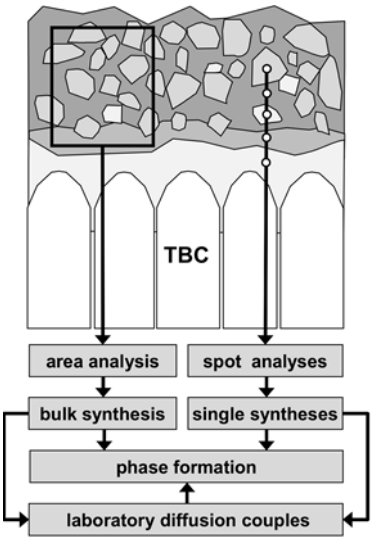

Fig.2

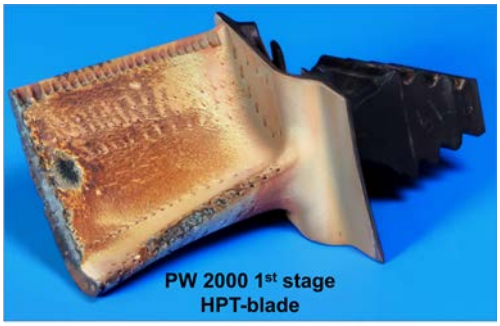

Fig. 3

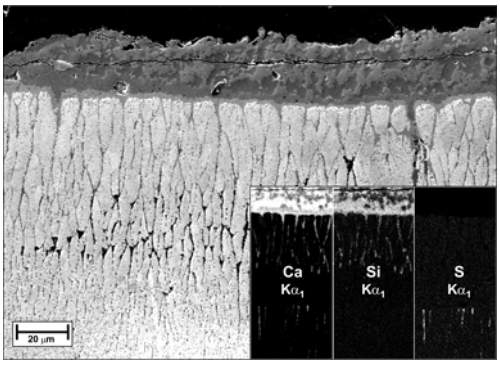

Fig. 4

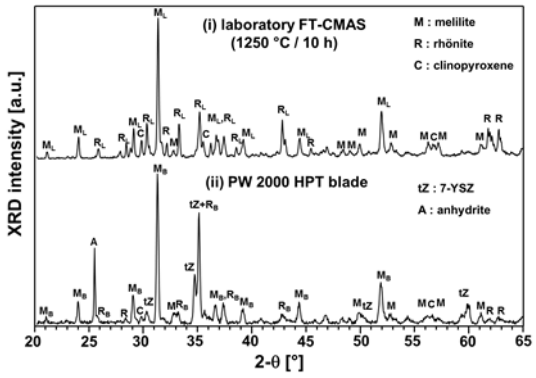

Fig. 5

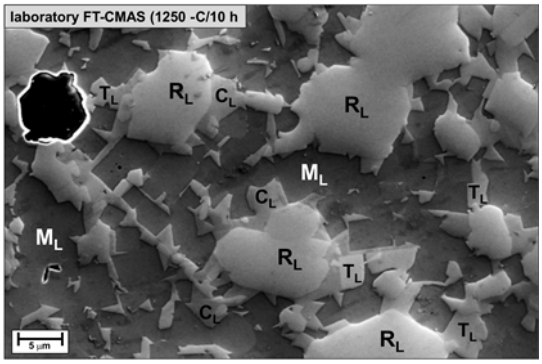

Fig.6

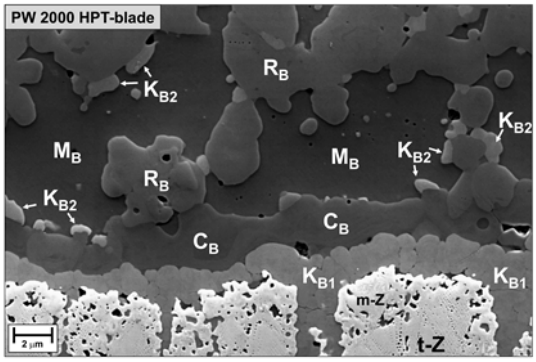

Fig. 7

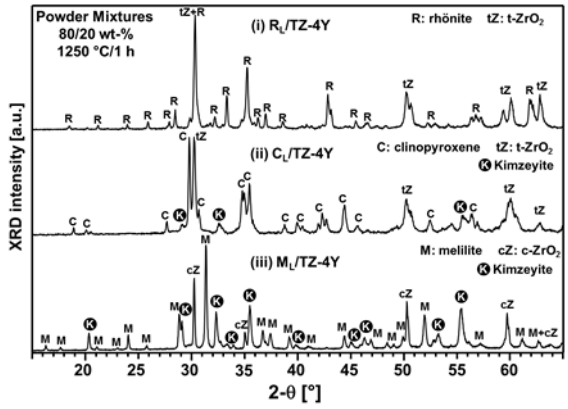

Fig.8

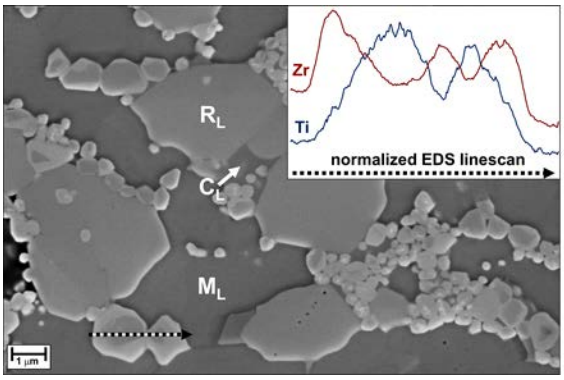

Table 1: Solid solutions in laboratory samples and in the CMAS-deposit of the PW 2000 HPT-blade

Rhönite (R_L; R_B)							
empirical formula[14] generalized rhönite structure	$Ca_4[(Mg,Fe^{2+})_8Fe^{3+}_2Ti_2]Al_6Si_6O_{40}$ $A^{[7]}_4[B^{[6]}_8C^{[6]}_2D^{[6]}_2]E^{[4]}_6F^{[4]}_6O_{40}$						
average EDS analysis [cation mol-%]	Mg	Al	Si	Ca	Ti	Fe	Zr
laboratory FT-CMAS : R_L	14.5	23.8	14.4	15.4	2.3	29.5	-
PW 2000 blade : R_B	14.6	25.0	15.7	18.1	1.8	24.8	0.0
cation allocation in generalized structure	B	E	F	A;B	D	B;C D;E	-
approximated rhönite$_{ss}$ R_L	$Ca_4[(Mg_{0.5}Fe^{2+}_{0.5})_8(Fe_2(Fe_{1.25}Ti_{0.75})]$ $(Al_{0.8}Fe_{0.2})_6(Al_{0.33}Si_{0.67})_6O_{38.5}$						
approximated rhönite$_{ss}$ R_B	$Ca_4[(Mg_{0.5}Fe^{2+}_{0.375}Ca_{0.125})_8(Fe_2(Fe_{0.75}Ti_{0.25})]$ $(Al_{0.917}Fe_{0.083})_6(Al_{0.25}Si_{0.75})_6O_{38.5}$						
Melilite (M_L ; M_B)							
empirical formula[17] generalized melilite structure	$Ca_2(Mg_xAl_{1-x})(Si_{1+x}Al_{1-x})O_7$ $A^{[8]}_2B^{[4]}T^{[4]}_2O_7$						
average EDS analysis [cation mol-%]	Mg	Al	Si	Ca	Ti	Fe	Zr
laboratory FT-CMAS : M_L	7.3	21.9	28.1	38.6	0.0	4.1	-
PW 2000 blade : M_B	7.1	19.7	27.2	43.0	0.0	3.0	0.0
cation allocation in generalized structure	B	T;B	T	A	-	B	-
approximated melilite$_{ss}$ M_L	$Ca_2(Mg_{0.4}Al_{0.4}Fe_{0.2})(Si_{1.4}Al_{0.6})O_7$						
approximated melilite$_{ss}$ M_B	$Ca_2(Mg_{0.35}Al_{0.48}Fe_{0.17})(Al_{0.65}Si_{1.35})O_7$						
Clinopyroxene (C_L ; C_B)							
empirical formula[22] generalized clinopyroxene structure	$Ca(Mg,Fe^{3+})[(Si,Al)_2O_6]$ $A^{[8]}B^{[6]}T^{[4]}_2O_6$						
average EDS analysis [cation mol-%]	Mg	Al	Si	Ca	Ti	Fe	Zr
laboratory FT-CMAS : C_L	7.8	15.5	29.4	24.4	2.6	20.3	-
PW 2000 blade : C_B	9.5	21.9	30.5	24.5	1.6	9.5	2.5
cation allocation in generalized structure	B	T;B	T	A	B	B	B
approximated clinopyroxene$_{ss}$ C_L	$Ca(Mg_{0.3}Fe_{0.6}Ti_{0.1})(Al_{0.3}Fe_{0.1}Si_{0.6})_2O_6$						
approximated clinopyroxene$_{ss}$ C_B	$Ca(Mg_{0.41}Fe_{0.41}Ti_{0.07}Zr_{0.11})(Al_{0.42}Si_{0.58})_2O_6$						

Ti-Garnet / Kimzeyite (T_L / K_{B1}, K_{B2}, K_L)							
empirical formula[24,27] generalized garnet structure	$Ca_3(Al,Fe,Ti)_2(Al,Si,Ti)_3O_{12}$ / $Ca_3(Fe,Ti,Zr)_2(Al,Fe,Si)_3O_{12}$ $A^{[8]}{}_3B^{[6]}{}_2T^{[4]}{}_3O_{12}$						
average EDS analysis [cation mol-%]	Mg	Al	Si	Ca	Ti	Fe	Zr
laboratory FT-CMAS : T_L	3.6	12.9	30.3	31.9	8.7	12.6	-
PW 2000 blade : K_{B1}	2.9	8.9	22.7	33.4	4.0	14.1	14.0
PW 2000 blade : K_{B2}	5.5	13.7	24.6	31.2	4.8	14.6	5.6
laboratory FT-CMAS/EB-YSZ diffusion couple : K_L	1.4	10.1	17.0	35.7	2.5	15.2	18.1
cation allocation in generalized structure	A	T;B	T	A	B	B;T	B
approximated Ti-Garnet$_{ss}$ T_L	$(Ca_{0.90}Mg_{0.10})_3(Al_{0.2}Fe_{0.47}Ti_{0.33})_2(Al_{0.20}Si_{0.80})_3O_{12}$						
approximated Kimzeyite$_{ss}$ K_{B1}	$(Ca_{0.92}Mg_{0.08})_3(Fe_{0.28}Ti_{0.16}Zr_{0.56})_2(Al_{0.23}Fe_{0.18}Si_{0.59})_3O_{12}$						
approximated Kimzeyite$_{ss}$ K_{B2}	$(Ca_{0.85}Mg_{0.15})_3(Fe_{0.59}Ti_{0.19}Zr_{0.22})_2(Al_{0.35}Si_{0.65})_3O_{12}$						
approximated Kimzeyite$_{ss}$ K_L	$(Ca_{0.96}Mg_{0.04})_3(Fe_{0.18}Ti_{0.10}Zr_{0.72})_2(Al_{0.27}Fe_{0.28}Si_{0.45})_3O_{12}$						
[8] [7] [6] [4] oxygen coordination numbers of cation sites							

Table 2 : Crystal chemistry of relevant phases from PW 2000 blade and laboratory experiments						
Crystal structure	**total cation sites [CN]**			**normalized to 3 [8]-sites**		
	[8]	[6]	[4]	[8]	[6]	[4]
Garnet[24,27]	3	2	3	3	2	3
Rhönite[14]	4*	12	12	3	2**+7**	3**+6**
Clinopyroxene[22]	1	1	2	3	2**+1**	3**+3**
Melilite[17]	2	0	3	3	0	3**+1.5**
Melilite-to-Garnet "conversion" scheme	(i) 1.5•[4] → 1.5•[6] (ii) 1.5•[6] + **0.5•[6]** → 2•[6]			3 **3**	**1.5** **2**	**3** **3**
Proposed reaction	**1.5 Melilite + 0.5 $Zr^{[6]}O_2$ → Kimzeyite**					
model #1: M_L**+ ZrO_2 → Kimzeyite; total Mg^{2+} allocated to site $B^{[6]}$	1.5 $Ca_2(Mg_{0.4}Al_{0.4}Fe_{0.2})(Al_{0.6}Si_{1.4})O_7$ + 0.6 ZrO_2*** → $Ca_3(Mg_{0.3}Al_{0.3}Fe_{0.1}Zr_{0.3})_2(Al_{0.3}Si_{0.7})O_{12}$					
model #2 : M_L**+ ZrO_2 → Kimzeyite; total Mg^{2+} allocated to site $A^{[8]}$	1.25 $Ca_2(Mg_{0.4}Al_{0.4}Fe_{0.2})(Al_{0.6}Si_{1.4})O_7$ + 1.25 ZrO_2*** → $(Ca_{0.833}Mg_{0.167})_3(Al_{0.25}Fe_{0.125}Zr_{0.625})_2(Al_{0.25}Si_{0.75})O_{12}$					
*coordination number CN=[7] ; **laboratory melilite (see also table 1) ; ***Y_2O_3 stabilizer not considered						